Optimal Hyper Elliptic Cambered Span Configurations for Minimum Drag

Prateek Ranjan[1], Phillip J. Ansell. [2] and Kai A. James [3]
University of Illinois at Urbana-Champaign, Urbana, Illinois 61801

The current study considers an analysis of hyper-elliptic cambered span wing configurations, optimized for minimum drag. This study encompasses a multi-dimensional design optimization approach wherein the wing geometries are optimized with respect to both span-load and spanwise camber to achieve minimum aerodynamic drag. A discrete vortex element method was coupled with a constrained gradient-based optimization routine to achieve these drag-optimal design configurations. Optimum drag configurations were obtained at a fixed design lift coefficient, as well as a fixed bending moment constraint. Navier-Stokes simulations were also performed, which revealed an L/D gain of 29.01% and 25.35% at design conditions, relative to an elliptically-loaded planar wing for the upward and downward cant configurations respectively. Different wake trace characteristics for the two hyper-elliptic cambered span configurations were observed along with surface flow features indicating different wake vortex and boundary-layer transition behaviors for the two hyper-elliptic cambered span configurations.

---

[1] Graduate Research Assistant, Department of Aerospace Engineering
[2] Assistant Professor, Department of Aerospace Engineering, Senior Member AIAA
[3] Assistant Professor, Department of Aerospace Engineering, Member AIAA

Nomenclature

A_{ij} = aerodynamic influence coefficient

AR = aspect ratio

b = span

b_e = elliptic wing span (m)

C_d = sectional drag coefficient

C_D = wing drag coefficient

C_l = sectional lift coefficient

C_L = wing lift coefficient

C_{L_α} = wing lift curve slope

C_f = skin friction coefficient

c = local wing chord (m)

$\bar{c}$ = mean aerodynamic chord (m)

c_{avg} = mean geometric chord

e = span efficiency factor

e_x = unit normal vector along x axis

h = wing camber height (m)

J = cost function

k_L = laminar kinetic energy

k_T = turbulent kinetic energy

l = length scale

M = number of discrete vortex elements

N = grid resolution

R = vortex influence radii

Re = Reynolds number

s = first layer cell height

s' = vortex semi-width

S = wing reference area (m^2)

T = turbulence intensity

$\bar{U}$ = mean velocity

y, z = cross-flow plane coordinates

α = angle of attack

α_0 = zero lift angle of attack

γ = normalized spanload

Γ = circulation strength

λ = Lagrange multiplier or taper ratio

ω = specific dissipation rate

ξ = x-component of vorticity

θ = local dihedral angle

Subscripts

i = index or induced

j = index

p = profile

pr = pressure

v = viscous

ref = reference

0 = zero order

1 = index

2 = second order or index

∞ = freestream

I. Introduction and Motivation

The quest for a faster and greener flight has challenged engineers since the early 1900's. Many early wing designs were inspired by nature's biological evolution of birds and insects [1, 2]. Efforts to understand wing aerodynamics have provided some of the earliest seminal works, such as Lanch-

ester's discussion on wake roll-up [3] and Prandtl's study on the minimum induced drag of planar wings [4].

A significant number of additional studies focused on energy efficient wing designs have also been documented in the literature. While early attempts to optimize planar wing configurations were fruitful [5–8], the inception of non-planar or out-of-plane wing configurations introduced the wing design community to a plethora of new design prospects that could lead to reductions in drag and increases in overall aerodynamic efficiency. As stated by Kroo [9], non-planar wing configurations can be categorized as multiple-wing designs, closed lifting systems, and wing tip devices. The gain in aerodynamic performance from one such class of non-planar wing configuration was presented by Whitcomb [10] in his study of wing-tip mounted winglets as a means to mitigate the trailing vortex system and associated induced drag. Use of various other forms of non-planar wing-tip extensions have also been reported in the literature [11–15], however the practical applicability of many of these devices to airplane design are limited due to associated increases in bending moments, susceptibility to flow separation, and poor flight stability. While, previous studies [16, 17] identified winglets to produce the best energy savings for non-planar wingtip device configurations, similar gains in aerodynamic performance have also been reported using planar wing-tip extensions [18, 19], Ogee and sheared tip configurations [20, 21]. Another class of non-planar wing system, designed primarily with induced drag considerations, is the multi-surface lifting system, termed as the best wing system by Prandtl in 1924 [22].The applications of the best wing system or the box wing to modern day flight requirements have also been studied recently by Demasi *et al.* [23].

A variety of passive approaches to mitigate vortex upset and reduce induced drag through span-load alteration with the use of spoilers and slats have been thoroughly studied by [24, 25]. However the use of lifting surfaces which actively perturb the trailing wake are often characterized with an increase in overall drag [26, 27]. The effectiveness of such mitigation methods have been investigated using theoretical models [28–30], experimental means of evaluations [31–34], as well as flight testing [35]. A recent study by Ranjan [36] and Wroblewski and Ansell [37] presents computational and experimental results of tailored span-loads of planar wing configurations for minimum induced drag, thus demonstrating the effectiveness of spanload alteration obtained using

a non-linear twist distribution.

Numerical optimization techniques have also been used to design optimal wing designs producing minimum drag and are reported extensively in the literature. Past studies such as [38–40] have discussed the use of numerical optimization for wing design. Sobieszczanski *et al.* [41] summarizes past studies which serve as the foundation to recent methods in wing design optimization. With the advances in computational engineering, especially high performance computing, the design optimization process of wing systems, and even full aircraft, has evolved to include multidisciplinary optimization considerations. Aero-structural considerations to wing design have been studied in [42–44], to name a few. Martins *et al.* [45] discussed the use an integrated multidisciplinary design optimization framework for the development of non-planar wing configurations using an inviscid flow formulation. A recent study by Nguyen *et al.* [46] explores the aerodynamic potential of cambered span configurations as a result of structural elastic response and reports a 5.9 % reduction in induced drag at design conditions.

The current study focuses on non-linear Hyper Elliptic Cambered Span (HECS) wing configurations, where the distribution of wing dihedral can be described using the equation of a hyperellipse. This study stems from the early work of Cone [47] who used potential theory to investigate the effectiveness of cambered span configurations. Significant gains over planar wing designs with span efficiency (e) greater than 1.5 were reported. However, Cone's study employed only inviscid models which did not account for drag contributions due to viscous effects.

HECS configurations and various other cambered span designs have been extensively reported in the literature. A study by Lazos [48] on cambered span configurations was inspired by wing geometries adapted from birds, especially seagulls, and reports significant reductions in the wing drag produced at a fixed lift coefficient by a HECS configuration, when compared to a baseline planar wing geometry. Similar observations have been reported from wind tunnel experiments in [49], wherein flow-field studies indicated an outboard shedding of trailing tip-vortex structures and lower drag for a downward cant design as compared to the upward cant geometry. An earlier study by Lowson [50] explored the induced drag characteristics of super-elliptic spanwise camber lines using a linear theory for optimum circulation distribution and concluded that the high camber close

to the wing tip, resulting in a vertical wing tip, is crucial for drag reduction. Lundry [51] presented a panel-based numerical method to compute induced drag characteristics of non-planar and swept wing configurations. Similarly, study by Lierch et al. [52] utilized lifting line and Euler methods to analyze the wings with varying dihedral distributions. Results from this study suggest that geometrically elliptic wings with spanwise camber are more efficient than planar designs with the same planform area. Pomeroy and Visser [53] investigated performance features of cambered span wing designs, where the projected span was less than or equal to that of the baseline planar design and concluded the non-planar designs to be more efficient than the baseline planar designs.

The current study presents an analysis of HECS wing configurations, which utilizes an optimized span loading and spanwise camber distribution to produce minimum aerodynamic drag under a fixed lift and bending moment constraint and with a fixed projected span. An extensive Navier-Stokes simulation approach is carried out to validate and asses the improved performance produced by the HECS configuration, and also to explain the underlying flow physics that are responsible for these gains. The object of the current study is to achieve a non-planar wing design based on the mathematical construct of the HECS configuration using a systematic multi-disciplinary design optimization framework, with both induced and viscous drag considerations. Such an integrated design approach was deemed necessary since previous discussions on cambered span wing configurations by [46–49] lacked such a design approach and also because of recent suggestions for HECS wing design made by Visser [54].

II. Theoretical Design Methods

A. Span-load Optimization Method

A discrete vortex element method with an embedded Trefftz plane analysis routine was used to compute the optimal span-loads for a given lift coefficient and HECS wing geometry. This design routine is based on the classic method discussed by Blackwell [55]. The design and embedded optimization routine is similar to those used in previous studies such as [56–59] and more recently in [37]. Though the design and optimization routine is the same as that in [37], the key elements of the routine are discussed here for the sake of completeness.

The non-linear cambered span profile is defined using the hyper-elliptic function, an approach similar to that of [48, 49, 52], and is expressed as:

$$z = h\left[1 - \left(1 - \left(\frac{2y}{b_{ref}}\right)^{n}\right)^{(1/n)}\right] \tag{1}$$

where h is the maximum wing height and b_{ref} is the reference projected span. The exponent n governs the camber gradient, where as the value of n increases the maximum gradient of the spanwise camber increases, with steeper variations in the slope of the wing dihedral moving outboard towards the wing tip. Fig. 1 illustrates the different camber profiles produced for varying values of n. Using Eq. 1, the z coordinates can be computed for varying spanwise locations at a given n and h, for either an upward cant (positive h) or downward cant (negative h).

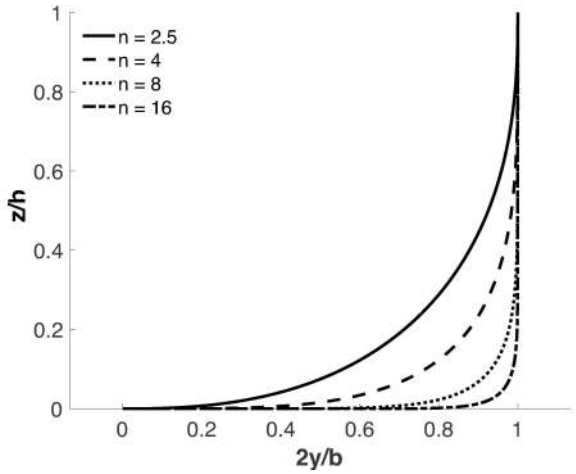

Fig. 1: Hyper-elliptic camber line profiles

Assuming a strip theory approach, the local bound circulation, Γ_j, of a wing section can be related to the spanload from the Kutta-Joukowski theorem and may be expressed as:

$$\frac{\Gamma_j}{V_\infty} = \frac{(C_l c)_j}{2} \tag{2}$$

where, the normalized spanload, γ_j, may be expressed as:

$$\gamma_j = \frac{(C_l c)_j}{c_{avg}} \tag{3}$$

At the Trefftz plane, the induced velocity at each control point can be expressed as a function of the lift distribution. Thus the circulation and cross-flow terms in the expression for induced drag can be expressed in terms of the spanload distribution:

$$C_{D_i} = \sum_{i=1}^{M} \sum_{j=1}^{M} \gamma_i \gamma_j s_i A_{ij} \tag{4}$$

Similarly, the lift expression is:

$$C_L = 2 \sum_{j=1}^{M} \gamma_j s_i \tag{5}$$

Here s_i is the normalized semi-width of a given vortex pair and A_{ij} is the aerodynamic influence coefficient matrix, both of which are a function of geometric configuration. The aerodynamic influence coefficient matrix A_{ij} is expressed as:

$$A_{ij} = \frac{c_{avg}}{4\pi} \left[\frac{(y' - s')}{R_1} - \frac{(y' + s')}{R_2} \right] cos(\theta_i - \theta_j) + \frac{c_{avg}}{4\pi} \left[\frac{z'}{R_1} - \frac{z'}{R_2} \right] sin(\theta_i - \theta_j) \tag{6}$$

Here, the coordinates of vortices along the span are expressed as:

$$y' = (y_i - y_j) cos(\theta_j) + \left[h \left[1 - \left(1 - \left(\frac{2y_i}{b_{ref}} \right)^n \right)^{(1/n)} \right] - h \left[1 - \left(1 - \left(\frac{2y_j}{b_{ref}} \right)^n \right)^{(1/n)} \right] \right] sin(\theta_j) \tag{7}$$

$$z' = -(y_i - y_j) sin(\theta_j) + \left[h \left[1 - \left(1 - \left(\frac{2y_i}{b_{ref}} \right)^n \right)^{(1/n)} \right] - h \left[1 - \left(1 - \left(\frac{2y_j}{b_{ref}} \right)^n \right)^{(1/n)} \right] \right] cos(\theta_j) \tag{8}$$

The corresponding vortex influence radii are expressed as

$${R_1}^2 = (z')^2 + (y' - s')^2 \tag{9}$$

$${R_2}^2 = (z')^2 + (y' + s')^2 \tag{10}$$

The dimensional vortex semi-width is expressed as:

$$s' = 0.5 \times \sqrt{(y_j - y_i)^2 + (z_j - z_i)^2} \tag{11}$$

To compute the optimum spanloads for the HECS configurations, the continuous spanwise camber was discretized into local sloped panels, where each panel was configured with a distribution of bound vortices (p). The paneling configuration of the wings remained the same for both upward and downward cant configurations. A grid independence study was performed to determine the required number of vortices per panel to achieve an asymptotic behavior in span efficiency. Fig. 2 represents the convergence trend for the upward cant HECS configuration. The span efficiency factor e is observed to be consistent with a fixed value for p greater than 8. Throughout this study, a total of 10 vortices per panel were used, while the total number of panels across the wing semi-span was set to 81.

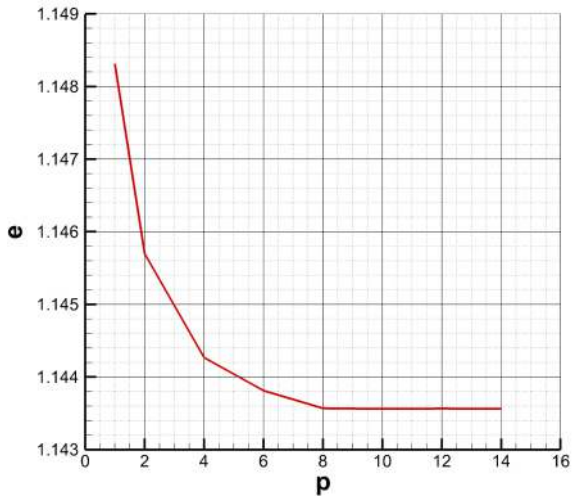

Fig. 2: Grid convergence characteristics for span-load optimization routine

The method of Lagrange multipliers was coupled to the vortex element routine in order to compute drag-optimal spanloads. An objective function for minimum induced drag at a fixed wing lift is expressed in augmented Lagrangian form as:

$$J = C_{D_i} + \lambda_{C_L}(C_L - C_{L_{ref}}) \tag{12}$$

where $C_{L_{ref}}$ is a prescribed lift coefficient for the wing and λ_{C_L} is the Lagrange multiplier for

the lift constraint. For the solution to be minimum, the sensitivities of the cost function J with respect to all independent variables must equal zero. Hence a system of linear equations can be formulated to solve for the spanload distribution (γ_j) that produces minimum induced drag for a fixed lift coefficient, which is expressed as:

$$\begin{bmatrix} \frac{\partial J}{\partial \gamma_j} \\ \\ \frac{\partial J}{\partial \lambda_{C_L}} \end{bmatrix} = [0] \tag{13}$$

Similar to the approach in [36, 46], the wing root bending moment constraint, which is commonly used as a surrogate for the wing weight, is added to the objective function, to produce:

$$J = C_{D_i} + \lambda_{C_L}(C_L - C_{L_{ref}}) + \lambda_{C_B}(C_B - C_{B_{ref}}) \tag{14}$$

where C_B is expressed as:

$$C_B = \frac{1}{2}\sum_{j=1}^{M} \gamma_j s_j \left(\frac{2y_j}{b}\right) \tag{15}$$

With the addition of the wing root bending moment, the system of equations to minimize the cost function now becomes :

$$\begin{bmatrix} \frac{\partial J}{\partial \gamma_j} \\ \\ \frac{\partial J}{\partial \lambda_{C_L}} \\ \\ \frac{\partial J}{\partial \lambda_{C_B}} \end{bmatrix} = [0] \tag{16}$$

Profile drag considerations were incorporated within the optimization routine using a strip theory approach, where the sectional drag coefficient is expressed using a quadratic equation, which models the parabolic variation of the local profile drag due to variations in the sectional lift [37, 51]. This quadratic expression for the profile drag was produced using a least-squares regression of the drag coefficient of an NACA 0015 airfoil, including the variation in the sectional profile drag produced with changing Reynolds number across the span. Based on the strip theory approach, the expression for total drag becomes:

$$C_D = \sum_{i=1}^{M}\sum_{j=1}^{M}\gamma_i\gamma_j s_i A_{ij} + \sum_{i=1}^{M}\left[C_{d,0_i} + C_{d,2_i}\left(\frac{\gamma c_{avg}}{c}\right)_i^2\right] \tag{17}$$

The final form of the objective function that minimizes the total wing drag under the constraints of a fixed lift coefficient and wing root bending moment hence becomes:

$$J = C_D + \lambda_{C_L}(C_L - C_{L_{ref}}) + \lambda_{C_B}(C_B - C_{B_{ref}}) \tag{18}$$

The remaining parameters used to prescribe the wing design are similar to those used in the study of Wroblewski and Ansell [37], and are listed in Table 1. The bending moment coefficient used in this study corresponds to a planar elliptically loaded wing at a fixed C_L and span.

Parameter	Value
C_L	0.439
C_B	0.279
$Re_{\bar{c}}$	450,000
Airfoil	NACA 0015
Taper ratio λ	0.5
Wing reference area (m^2)	0.1287

Table 1: Design constraints

The spanload optimization approach was used with a parametric variation across a grid in n and h to better understand the design space characteristics, such as number of local optimum and their respective locations. Knowledge of such parameters acted as a precursor to the type of gradient based optimization algorithm used later. Fig. 3 represents the carpet plot of C_{D_i}, C_{D_p} and C_D, plotted in the $n-h$ plane, using the cost function provided in Eq. 18. As expected, the induced drag tends to decrease with an increase in wing arc length associated with larger values of n and h. Such a configuration is consistent a conventional winglet design for the largest reductions in induced drag. On the other hand, the profile drag is observed to increase with wing arc length through increasing n and h. This result is expected as the wetted area increases with increases in arc length.

The carpet plot for the total drag generally suggests high aerodynamic drag for small values of n and increasing maximum cambered-span height, which thus corresponds to the individual trends of profile and induced drag. Based on Fig. 3, a global minimum exists at $2h/b = 0.04063$ and $n = 5.82$. The optimum design configurations producing minimum aerodynamic drag are summarized in Table 2. It should be noted that the vortex panel method and the optimization routine predict the same optimum camber profile for both upward and downward camber configurations due to the fixed wake assumption of the Trefftz plane analysis and neglecting viscous wake interactions. A similar observation was made by Cavallaro *et al.* [60] and Depace *et al.* [61] wherein a configuration-invariant Euler-Lagrangian equation framework was discussed assuming a fixed wake, as an alternative to the panel based methods such as that used in the current study, to obtain the potential flow equations.

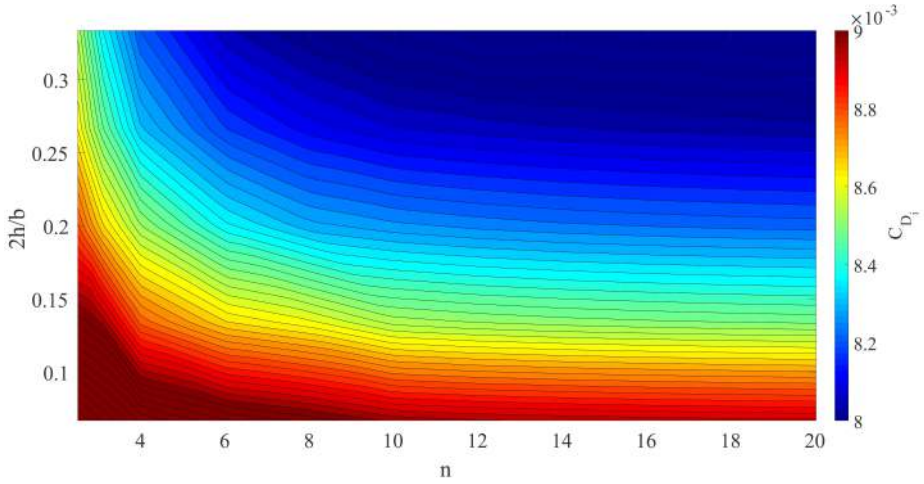

(a) C_{D_i}

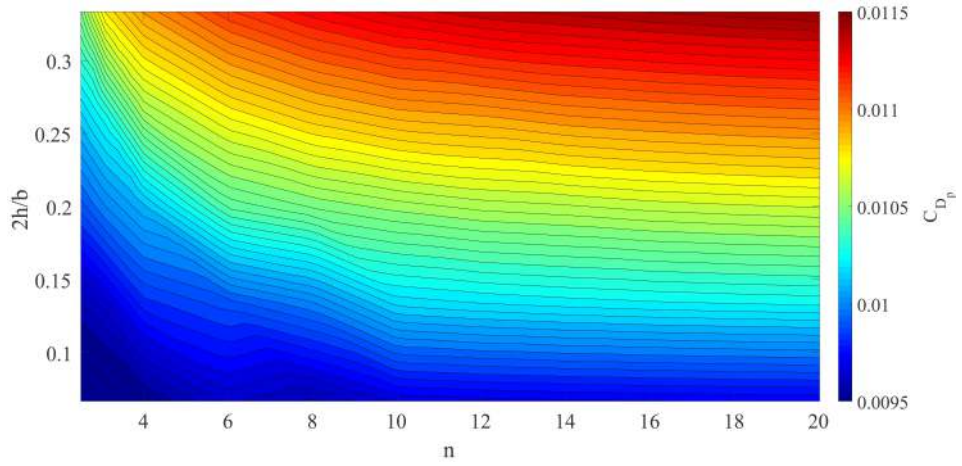

(b) C_{D_p}

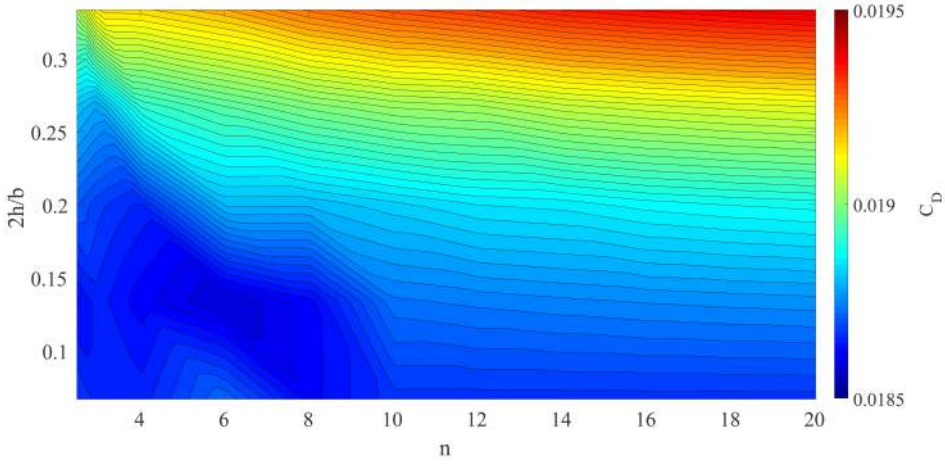

(c) C_D

Fig. 3: Carpet plots for non-planar wing configurations

Fig. 4 presents the optimal spanloads for all three wing configurations both with and without the wing root bending moment constraint. The planar wing follows an elliptic spanload since it is optimized based on a fixed C_L and span. The upward and downward HECS configurations have same optimal spanloads. However when the wing root bending moment constrain is on, the HECS wings have a higher loading at the root compared to the elliptic spanload. Conversely, a lower loading at the root is observed when the wing root bending moment constrain is turned off in the optimization routine. Such differences in the spanload distribution observed between Figs. 4(a) and 4(b) indicate that the wing root bending moment constraint is indeed active in the optimization formulation. Hence, all wing design configuration characteristics presented hereafter are for the wing root bending moment constrain on. Table 2 indicates a 2.01 % decrease in C_D of the two HECS configurations from the baseline elliptic wing. Table 3 lists the C_D for the three wings at zero lift condition. Given that the spanload at the design condition is produced by implementing a spanwise geometric twist, the basic lift distribution at $C_L = 0$, is nonuniform. As a result, even at the wing zero-lift condition, a nonzero induced drag coefficient is produced. Greater reductions in $C_{D_{i_0}}$ are observed for the two HECS wings when compared to the planar baseline wing.

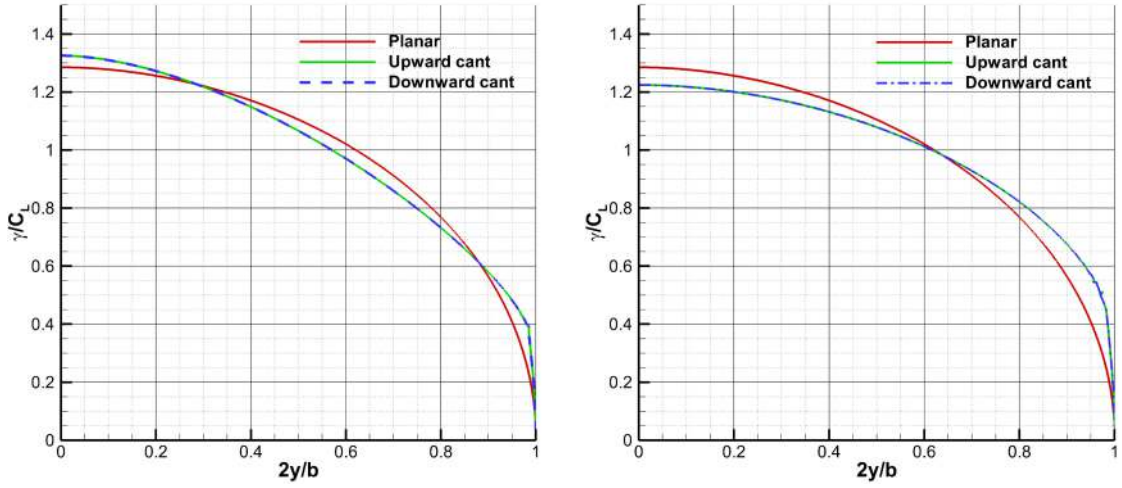

(a) WRBM contrain on

(b) WRBM constrain off

Fig. 4: Optimal spanloads

Configuration	C_{D_i}	C_{D_p}	C_D	e	AR
Planar elliptic	0.00942	0.00929	0.01871	1.00	6.5
Upward cant	0.00840	0.00991	0.01831	1.129	6.5
Downward cant	0.00840	0.00991	0.01831	1.129	6.5

Table 2: Predicted drag characteristics of baseline elliptic and drag-optimal HECS configurations

Configuration	$C_{D_{i0}}$	$C_{D_{p_0}}$	C_{D_0}
Planar elliptic	0.00451	0.00899	0.013503
Upward cant	0.00110	0.00963	0.010630
Downward cant	0.00110	0.00963	0.010630

Table 3: Predicted drag characteristics of baseline elliptic and drag-optimal HECS configurations at $C_L = 0$

B. Gradient-based Optimization

The optimization routine discussed in the previous section provided a grid-based approach wherein drag characteristics were computed across a set of prescribed values in the wing degree of camber (exponent n) and wing maximum height, for a constant reference area and projected span. The interior point method of optimization [62] was used in the current study to minimize the objective function with n, h and γ_j as independent variables. Using this method, the $j+2$ dimensional optimization formulation becomes:

$$\begin{aligned}
\underset{h,n,\gamma_j}{\text{minimize}} \quad & C_D = \sum_{i=1}^{M}\sum_{j=1}^{M}\gamma_i\gamma_j s_i A_{ij} + \sum_{i=1}^{M}\left[C_{d,0_i} + C_{d,2_i}\left(\frac{\gamma c_{avg}}{c}\right)_i^2\right] \\
\text{subject to} \quad & C_L = 2\sum_{j=1}^{M}\gamma_j s_i = 0.436 \\
& C_B = \frac{1}{2}\sum_{j=1}^{M}\gamma_j s_j\left(\frac{2y_j}{b}\right) = 0.046 \\
& n \geq 2.1
\end{aligned} \tag{19}$$

The two equality constraints in the formulation above are based on the baseline wing configuration experimentally studied by Wroblewski and Ansell [37]. The inequality constraint for n limits the design space to strictly hyper-elliptic camber-line configurations.

The geometric parameters for the two HECS configurations obtained using the gradient-based optimization routine are summarized in Table 4, with the minimum drag configuration summarized in Table 5. The gradient-based optimization produced a slightly larger drag reduction of 3.0 % vs. 2.01 % from the grid search method. The authors attribute the difference in optimal configurations due to the relatively coarse grid resolution utilized when performing the grid search. No differences in performance of the upward and downward cant configurations were observed, since the spanloads for each candidate design during optimization were computed using the potential flow model subroutine discussed earlier. As such, the differences in drag between the upward and downward cant configurations associated with complex viscous effects or wake roll-up were not resolved.

Configuration	C_{D_i}	C_{D_p}	C_D	e	AR
Planar elliptic	0.00942	0.00929	0.01871	1.00	6.5
Upward cant	0.008231	0.00991	0.01814	1.152	6.5
Downward cant	0.008231	0.00991	0.01814	1.152	6.5

Table 4: Predicted drag characteristics of baseline elliptic and drag-optimal HECS configurations

Configuration	n	$2h/b$
Upward cant	6.02	0.04063
Downward cant	6.02	0.04063

Table 5: Geometric parameters for drag-optimal HECS configurations

Fig. 5 illustrates the computer generated geometries for the two HECS configurations and the baseline planar configuration.

(a) Upward Cant (b) Downward Cant (c) Planar

Fig. 5: Non-planar and planar elliptic configurations

III. Navier-Stokes Simulation Method

OpenFOAM, a three-dimensional open-source CFD package, was used as the flow solver in the current study to perform Navier-Stokes simulations of the HECS wing flow fields. This package is compiled as an unstructured finite volume solver [63, 64] which contains a large number of sub-routines for different flow regimes [65].

OpenFOAM consists of an object-oriented architecture wherein solvers, operators and turbulence models are assigned to classes. This setup allows for a better understanding of the underlying source code, which is responsible for simulating flow physics as compared to other CFD toolkits written in procedural languages [64, 66]. The effectiveness and accuracy of such a programming structure has been reviewed by [66–68] and the accuracy and scaling characteristics of OpenFOAM as a CFD solver has been discussed comprehensively in [69–74].

The numerical setup used to analyze the HECS and planar wing configurations are similar to those used in [36]. However, key details of the turbulence model used and pre-processing steps are briefly discussed in the following sections.

A. Mesh generation

Two different mesh generation strategies were used between the planar and HECS wing configurations due to different geometric gradients along the span. The main differences lied in the wing surface mesh resolution where more cells were added to resolve the non-planar section in both HECS wing configurations. For all cases, a hemispherical unstructured computational domain with a wing-root symmetry plane was generated using a third-party mesh generator Pointwise. An ini-

tially structured mesh consisting of hexahedral cells was diagonalized to achieve better control on volumetric cell growth off the surface (Fig. 6). This type of surface mesh treatment resulted in better mesh quality in terms of cell orthogonality and skewness. A far-field boundary was placed at $x/\bar{c} = 300$, with the wing root section of the quarter chord used at the origin. To resolve the wall boundary layer, a y^+ value close to unity was maintained at the surface for all wing designs using tetrahedron cells in the boundary layer. The anisotropic cells at the boundary layer allowed for better control over y^+ values since first cell height could be maintained all over the geometry. Fig. 7 shows the volumetric cell growth and transition from near-wall tetrahedrons to far-field prisms. A wake baffle was configured to extend from the wing trailing edge to $x/\bar{c} = 20$ for all geometries.

(a) Planar surface

(b) Non-Planar surface

Fig. 6: Surface mesh

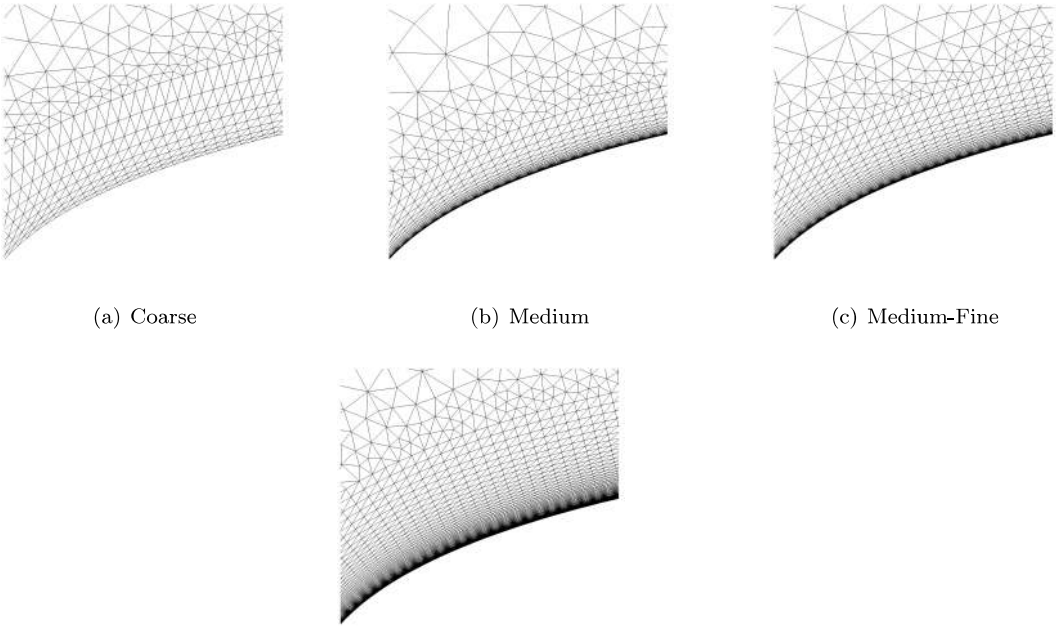

(a) Coarse (b) Medium (c) Medium-Fine

(d) Fine

Fig. 7: Near-wall grid resolution on the upper surface of the root wing section for the elliptic wing

A grid convergence study for the elliptically loaded trapezoidal wing was conducted with meshes of different near-wall anisotropic cell densities. All simulations were performed at $Re_c = 450,000$ and a design $C_L = 0.439$, similar to [36]. Grid parameters used for the elliptically loaded planar wing (hereafter elliptic wing) are listed in Table 6.

Grid Number	Grid	Resolution	Growth Rate
1	Coarse	4.5×10^6	1.5
2	Medium	6×10^6	1.3
3	Medium-Fine	12×10^6	1.2
4	Fine	21×10^6	1.1

Table 6: Grid Convergence Study Parameters for Planar Elliptic wing.

For all solutions, a transition model was used, as will be discussed in Section III. B. The grid convergence characteristics for the baseline planar elliptic wing are shown Fig. 8. With the increase in grid resolution, especially in the boundary layer region, the numerical solution is expected to

asymptotically approach the true numerical solution. While grid number 1 results in the use of wall-functions and failure to predict transition, grid numbers 3 and 4 result in a stable solution with agreeable flow transition effects. Considering the similarity in accuracy between grids 3 and 4, and the necessary increase in computational cost, grid number 3 is chosen for the baseline planar wing configuration. Similar trends in grid convergence were observed for both upward and downward cant HECS configurations.

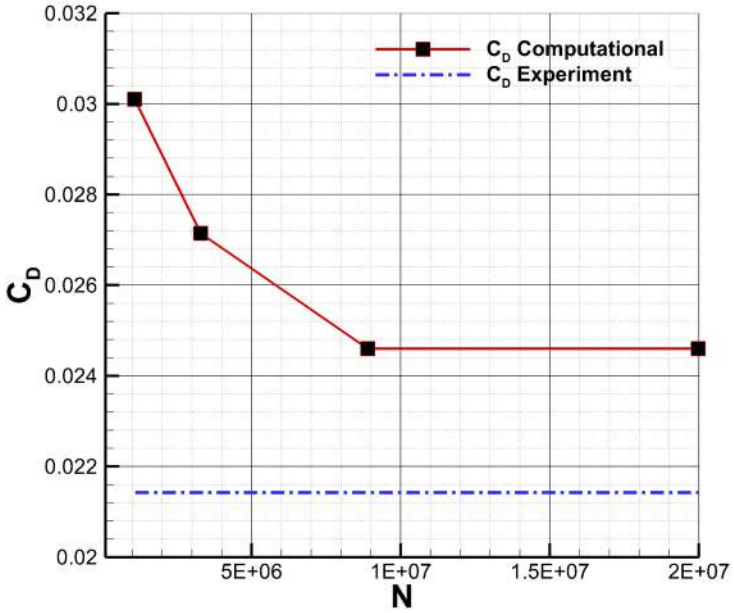

Fig. 8: Grid convergence for elliptic wing

B. Turbulence modeling

A comprehensive review of various one-, two- and three-equation turbulence models within OpenFOAM framework can be found in [75]. The current study employs a three equation eddy-viscosity model wherein an additional transport equation is used to predict the onset of transition, which is added to the two equation $k-\omega$ framework [74]. The third transport equation quantifies the laminar kinetic energy [76], k_L, which in-turn corresponds to the magnitude of low frequency velocity fluctuations that are precursors to flow transition. The $k-k_L-\omega$ turbulence model has been derived as a single point turbulence model from [75] and has been shown to predict flow transition effects to a reasonable degree of accuracy, as discussed in [36, 77]. A revised formulation of the $k-k_L-\omega$ turbulence model proposed by [78] is used in the current study.

C. Initial conditions and solution technique

The aerodynamic characteristics for the HECS and planar wing designs were resolved for a range of angles of attack at $Re_{\bar{c}} = 450,000$. A more exhaustive computational domain with added near-wake baffles was used for analyzing the three wings at the design $C_L = 0.439$. Resolving this portion of the flow field allowed for the near-field wake structure to be analyzed. A symmetry plane in the computational domain was used to model the semi-span for the wing geometries, which assisted with reducing the required computational expense. All simulations were analyzed at zero gage-pressure. At the inlet, $\bar{U} = v_{x,\infty}$ and $\nabla p_{x,\infty} e_x = 0$ were used for velocity and pressure fields. A no-slip or wall boundary condition was imposed on the wing surface. At the outlet, the velocity and pressure field boundary conditions were $\nabla \bar{U} e_x = 0$ and $\bar{p} = p_\infty$, respectively. The turbulence model terms k_L and k_T being functions of velocity, were assigned as zero gradient boundary conditions on the wing surface. Initial values for k_L and ω were computed using methods described in [76]. Based on the freestream turbulence intensity of 0.1% from the experiments of Wroblewski and Ansell [37], the turbulent kinetic energy was calculated using the expression [78]:

$$Tu_\infty = \frac{\sqrt{2/3 k_T}}{U_\infty} \tag{20}$$

The simulations were performed using a collocated unsteady RANS-based approach wherein all scalars are face-interpolated to the cell centers. A large time step and adjustable Courant number transient solver based on the PISO algorithm was used for pressure-velocity coupling. This simulation approach has shown to be more advantageous over the more segregated schemes such as SIMPLE and SIMPLEC, especially for low-Reynolds number flows [76, 79]. The solver equations were discretized using Gaussian integration schemes along with a cubic interpolation scheme to interpolate values from the cell center to the cell face. First order upwind schemes were used to obtain a stable solution, and thereafter a switch to a second order upwind scheme was made for the moment terms.

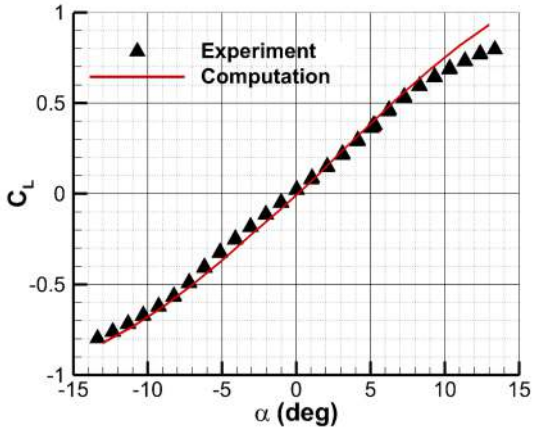

(a) C_L Characteristics

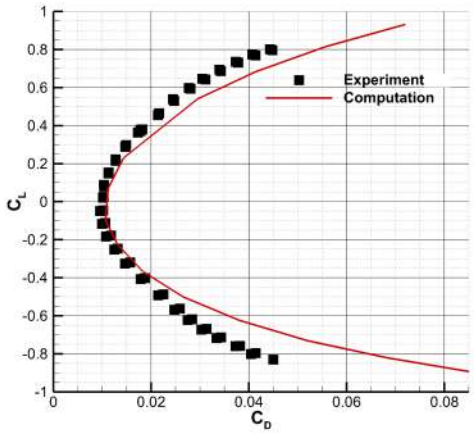

(b) C_L and C_D polar

Fig. 9: Performance characteristics validation for the planar elliptic wing

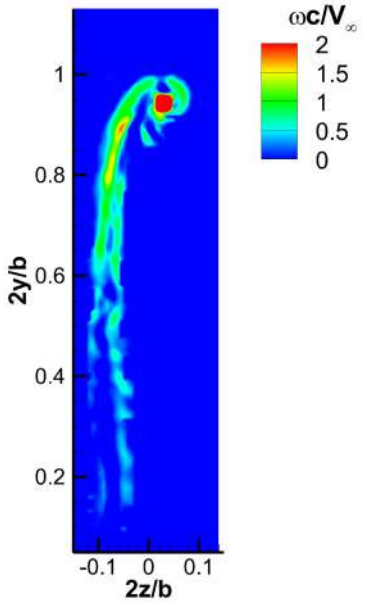

(a) Experiment

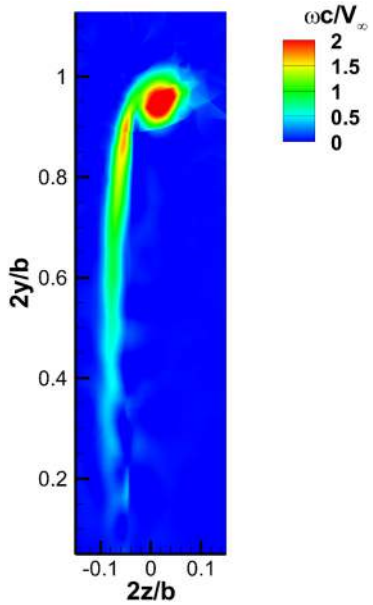

(b) Computational

Fig. 10: Vorticity contours for the planar elliptic wing at $x/\bar{c} = 4.6$

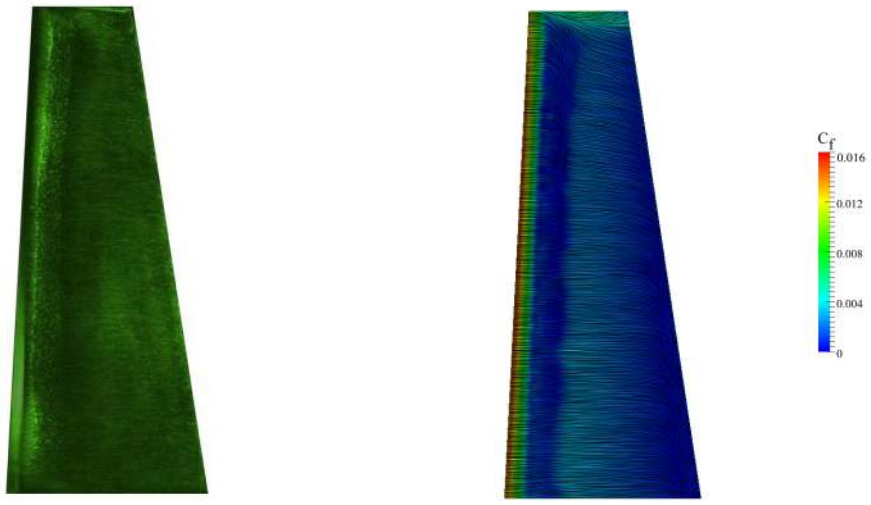

(a) Experiment (b) Computational

Fig. 11: Surface flow visualization for the planar elliptic wing at design C_L

A validation of wing lift and drag performance obtained from Navier-Stokes simulations was performed with the experimental data from [37]. Fig. 9 indicates a good agreement between the simulations and experimental performance. The relative difference observed at higher angles of attack are found to be consistent with previous studies found in the literature [80]. In addition to the wing performance, the flow characteristics at the wing design conditions are predicted with reasonable accuracy in this study. Similarities in the wake vorticity contour of simulations and experiment measured at $x/\bar{c} = 4.6$ are shown in Fig. 10. Key wake vorticity features such as the global characteristics and local maxima observed near the wing tip, observed in Fig. 10 (a) are resolved in the simulated vorticity contour of Fig. 10 (b). The experimental surface flow data from [37] is also compared with the predicted surface flow visualization obtained at design C_L for the baseline planar elliptic wing using surface line integral convolution of C_f, shown in Fig. 11, and similarities in the transition bubble characteristics are observed.

IV. Results and discussion

To asses the performance characteristics of the HECS configurations over a wide range of angle of attack, a series of simulations were carried out for the two configurations and compared with the

baseline planar elliptic wing. All simulations for the upward and downward HECS configurations were carried out using the same flow conditions, where the wing angle of attack was referenced to the angle of attack local to the wing root.

Fig. 12 represents the C_L characteristics for the two HECS configurations along with the baseline planar wing. For positive angles of attack, the upward cant configuration is characterized by a higher C_L when compared to the downward cant and planar wings. A higher C_{L_α} for the upward cant HECS wing is also observed, corresponding to an increase in the effective aspect ratio of the wing. Though this should be true for the downward cant HECS wing, the relatively lower C_{L_α} may be attributed to the negative lift component produced across the wingtip device by the downward cant configuration [51]. The trend also indicates a similar α_0 for both the baseline planar and upward cant HECS wing and a positive α_0 (≈ 0.2 degrees) for the downward cant HECS wing. For lower angles of attack, the baseline planar wing configuration exhibits higher C_L when compared to the two HECS configurations. Fig. 12(b) represents the C_L characteristics near the design point ($C_L = 0.439$). Clearly, as observed, the upward cant configuration exhibits the smallest root angle of attack required to produce the design C_L when compared to the downward cant and planar wings.

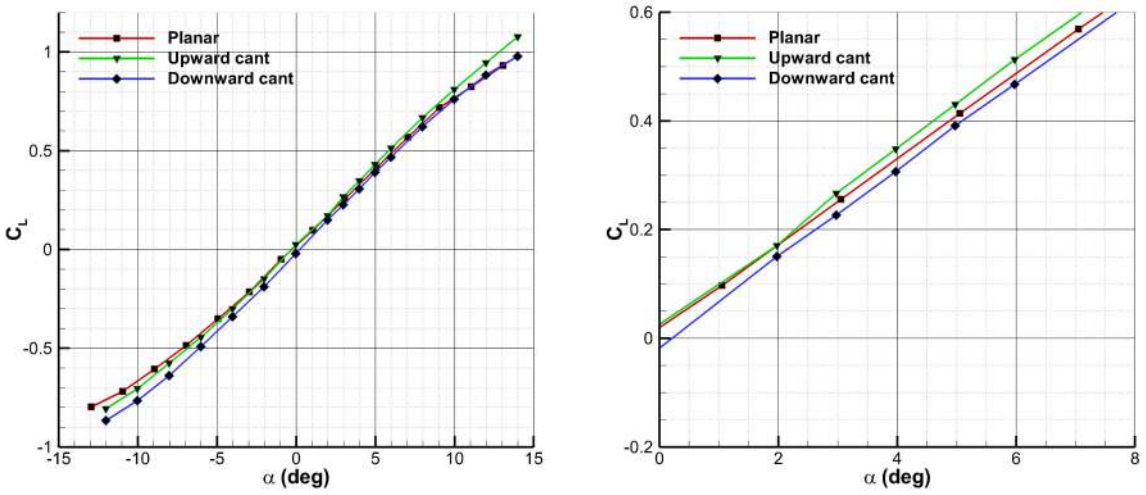

(a) (b)

Fig. 12: C_L characteristics

Fig. 13 represents the C_L vs. C_D characteristics for the three wing configurations. The trends indicate the two HECS wings outperform the baseline planar wing at the design as well as off-

design C_L conditions. The upward cant HECS wing is observed to produce the lowest amount of aerodynamic drag at the design C_L. However, for $C_L \leq 0.439$, the downward cant configuration produces the lowest drag. For $C_L \geq 0.439$, the upward cant HECS wing is observed to produced less drag as compared to the downward cant HECS wing. Interestingly, for low angles of attack, the baseline planar wing is expected to produce the lowest C_D, due to its lower surface wetted area and since the profile drag contribution plays a more significant role at lower values of C_L. However, Fig. 13 indicates the HECS wings to outperform the planar wing throughout the full drag polar. Such reductions in C_{D_0} are attributed to the reductions in $C_{D_{i_0}}$ as observed earlier in Table. 3. A similar trend in C_D reductions produced by a HECS configuration was observed in the study of Lazos [48].

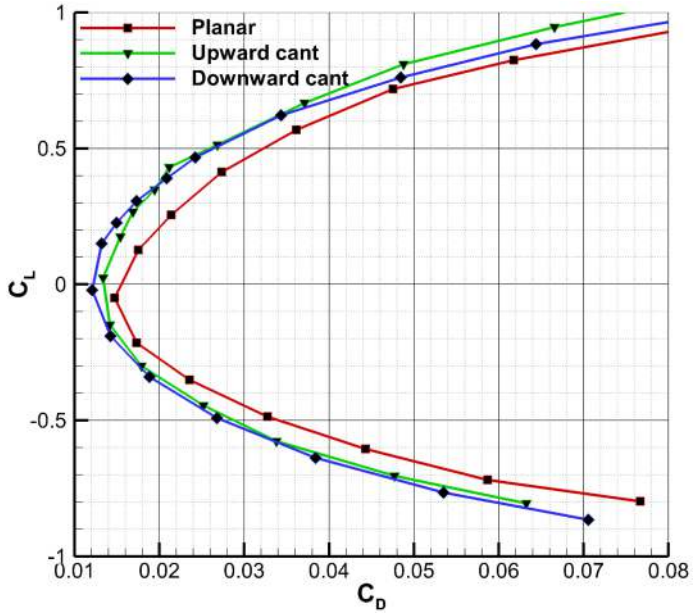

Fig. 13: C_L vs. C_D characteristics for the three wings

The aerodynamic efficiency of a lifting body is generally assessed from its L/D characteristics. Fig. 14 represents the overall L/D characteristics for the two HECS wings in comparison to the baseline wing configurations. The highest L/D at design point of $C_L = 0.439$ is obtained from the upward cant HECS wing, with a 29.01 % increase from the baseline planar wing. This case is followed by the downward cant HECS wing with a 25.35 % increase in L/D. Corresponding to the trends observed in Fig. 14, the baseline planar wing has the lowest L/D at and around the design point.

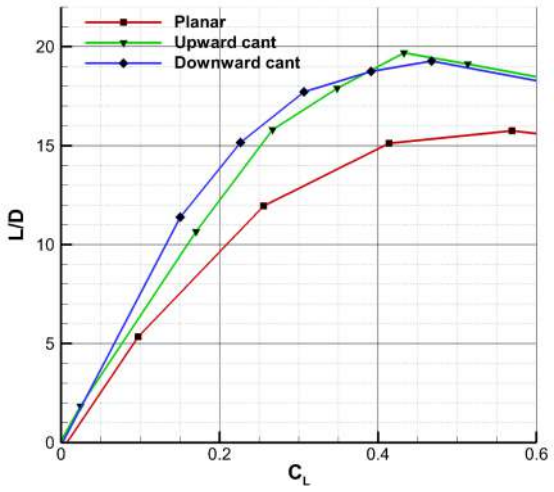

Fig. 14: L/D characteristics

The observed trends in L/D characteristics of the HECS wings in this study are similar to experimental results for the HECS wing of Lazos [48, 49]. However, Lazos reported greater reductions in C_D from an upward cant HECS wing compared to a downward cant HECS wing for the entire drag polar whereas in the current study, the upward cant configuration produces lower C_D in the proximity of the design condition only. Such differences may be a result of the variations in wing planform and trailing edge sweep between these studies since Lazos's study was based on a HECS configuration with a mean sweep angle of 19.98 degrees.

A near-field wake analysis was performed to study the immediate wake structures, which dictates the wake roll-up behavior of all three wings. The wake vortex structure for the two HECS configurations were resolved at two near-field stations and compared with that produced by the baseline planar elliptic wing. All wake survey locations are referenced to the wing quarter chord location and the vorticity magnitude in each case is normalized by the maximum wake vorticity magnitude specific to design configuration. Fig. 15 shows the wake vorticity contours at $x/\bar{c} = 2$. All three configurations exhibit a tip vortex which is due to the aggressive decrease in bound circulation local to the tip. Fig. 15 indicates two key differences in the near-field wake vorticity profiles for the three wings. Firstly, a significant decrease in vortex core strength is observed for the HECS wings when compared to the baseline planar wing. This decrease in vorticity is known to correspond to reductions C_{Di} at the design condition shown. Secondly, the two HECS wings are characterized

with different wing tip roll-up characteristics, with an inboard tip vortex being shed for the upward cant HECS wing and an outboard tip vortex being shed for the downward cant HECS wing. Fig. 16 represents the wake vorticity contours at $x/\bar{c} = 4$. Similar to the observations from Fig. 15, a reduction in vortex strength (both at tip and inboard stations) and different tip vortex shedding characteristics are observed in Fig. 16 between different wing configurations. The decrease in vorticity magnitude for the downward cant HECS wing can thus be expected to produce the lowest C_{D_i} characteristics for $\alpha \geq 0$.

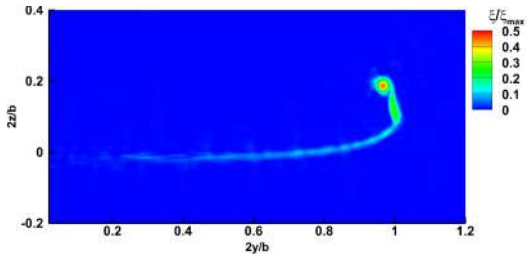

(a) Upward cant HECS

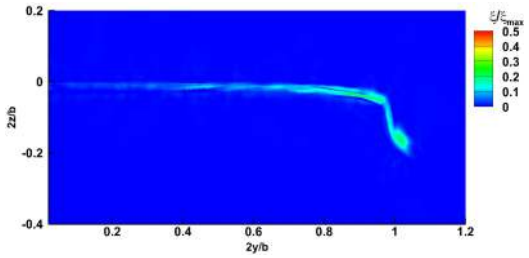

(b) Downward cant HECS

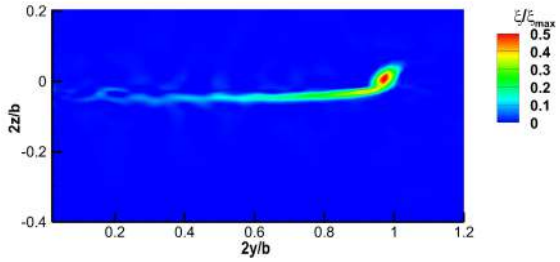

(c) Planar baseline

Fig. 15: Wake vorticity at $x/\bar{c}$=2

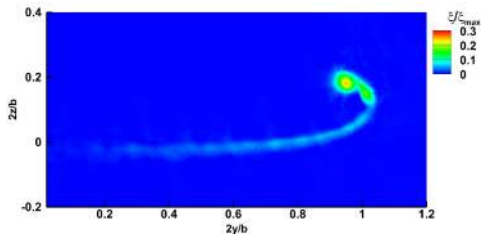

(a) Upward cant HECS

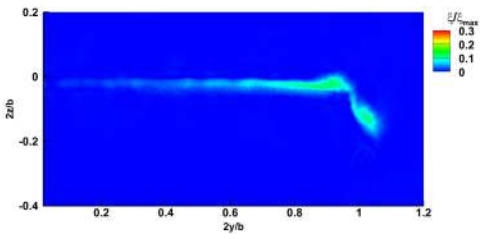

(b) Downward cant HECS

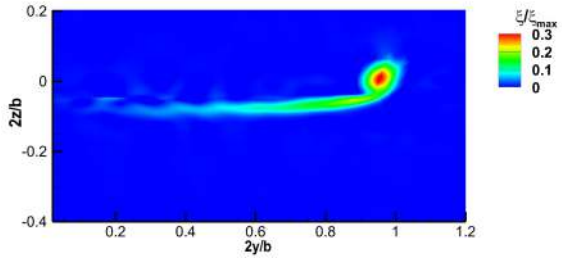

(c) Planar baseline

Fig. 16: Wake vorticity at $x/\bar{c}$=4

Fig. 17 represents the wake iso-contours for the three wing configurations. Adding on to the difference in wake characteristics observed earlier in Figs. 15 and 16, Fig. 17 indicates different wake vortex characteristics for the three wings up to $x/\bar{c}$ =20, downstream to the wing. For instance, the baseline elliptic wing is characterized by a rapid and immediate wake roll up when compared to the two HECS wings. While both upward and downward cant HECS wings exhibit similar wake roll-up rates, the tip vortex geometry is different for the two wings. The upward cant HECS wing exhibits a much smaller tip vortex when compared to the planar wing. However, for the downward cant HECS wing, the shape of the vortex core appears to be characteristically different than the other two wings due to the outboard shedding of tip vortex seen earlier in Figs. 15 and 16.

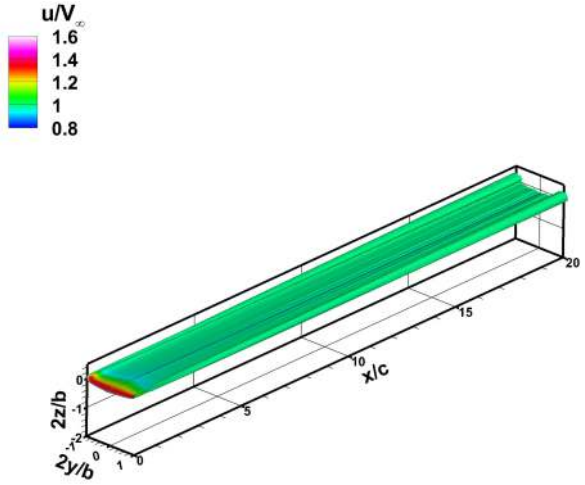

(a) Upward cant HECS

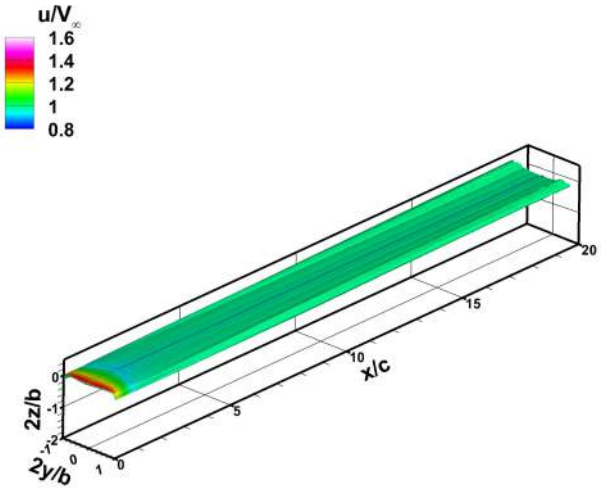

(b) Downward cant HECS

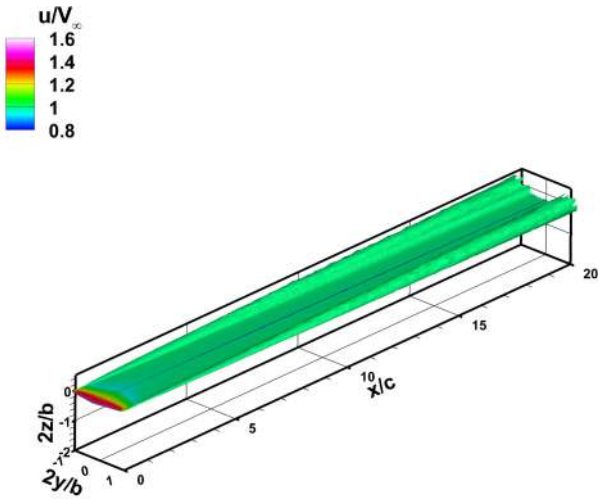

(c) Planar baseline

Fig. 17: Wake iso contours for three wing configurations

.

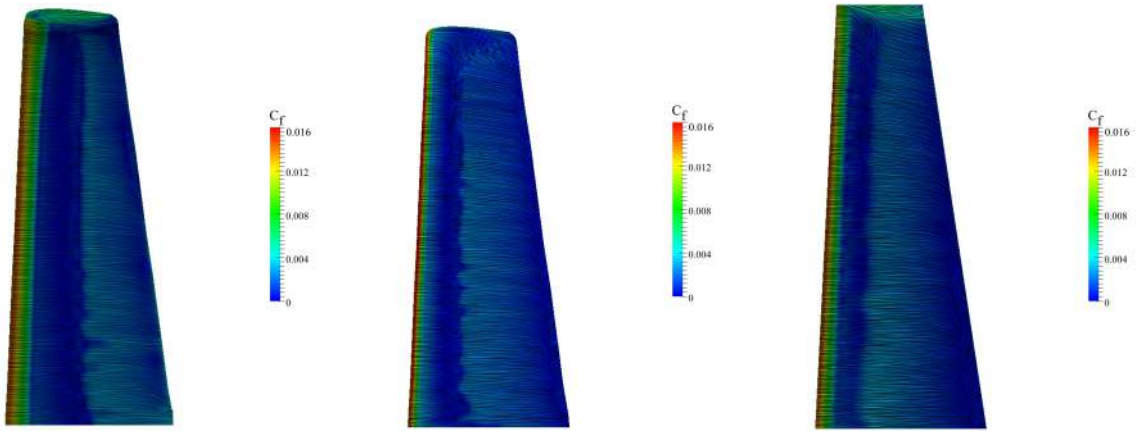

(a) Upward cant HECS (b) Downward cant HECS (c) Baseline planar

Fig. 18: Wing surface skin friction coefficient at design C_L

The C_f contours for the three wing configurations are presented in Fig. 18. The largest laminar separation bubble (region over which $C_f \leq 0$) is observed for the upward cant HECS wing while the baseline planar wing exhibits a smaller transition zone that is placed farther upstream. The surface flow visualization suggests no significant span-wise flow for contribution across the upper surface of the HECS wings. Interestingly, the transition characteristics are similar for the downward cant and the baseline planar configuration. However, for the upward cant configuration, the onset of transition is observed to be further downstream. Table. 7 presents the pressure and viscous drag contributions for the three wings at the design C_L. The C_{D_v} for the upward cant configuration is the lowest amongst the three wings which corresponds to the largest laminar pre-transitional region (Fig.18(a)), while similar C_{D_v} characteristics are observed between the baseline and downward cant configurations. The downward cant configuration is characterized with the lowest $C_{D_{pr}}$ which is due in large part to the reduction of wake vorticity observed earlier in Figs. 15 and 16.

Configuration	C_D	$C_{D_{pr}}$	C_{D_v}
Planar elliptic	0.02879	0.02160	0.00718
Upward cant	0.02173	0.01795	0.00378
Downward cant	0.02298	0.01589	0.00709

Table 7: Pressure and viscous drag characteristics of baseline elliptic and drag-optimal HECS configurations

V. Conclusions

A set of minimum-drag hyper elliptic cambered span wing configurations were developed using a potential flow model and analyzed using Navier-Stokes simulations. Optimal HECS wing design configurations were obtained using a grid search method wherein the influence of maximum span height h and hyper-elliptic exponent n on both induced and profile drag were discussed. A more optimal design configuration was obtained from a gradient-based optimization routine. A net reduction in drag of 3 % was predicted from the lower fidelity method. Performance analysis based on unsteady Navier-Stokes simulations at the design point revealed a 29.01% gain in L/D from the upward cant configuration over the baseline planar elliptic configuration. The downward cant configuration indicated a L/D gain of 25.35% relative to the baseline wing. Wake vorticity contours at two different stations downstream of the three wings revealed different tip vortex characteristics for the upward and downward cant HECS wings relative to the planar baseline wing. The difference in vorticity features in the wake reflected a difference in induced drag characteristics, since this variation in wake vorticity produces different downwash characteristics in the near-field region. Given that the potential flow model assumed a fixed wake, the different wake roll-up effects produced by the upward and downward cant configurations were not captured, which would otherwise lead to variations in C_D between these two wings when using this finite vortex element method. At the design point, the downward cant HECS wing produced the lowest pressure drag as compared to the upward cant and planar baseline wings. The lowest viscous drag was produced by the upward cant HECS wing which was in accordance with the largest laminar flow region observed in the C_f contour

plots. The application of the design and optimization framework of the current study is envisaged as a stepping stone towards the development of an integrated potential flow and three dimensional incompressible Navier-Stokes solution based optimization framework ans its application towards the design of sailplane and low speed commercial aircraft wings. Such an integrated optimization framework will not only be synonymous to the current state of the art in low speed wing design but may also result in an improvement over the current conventional wing designs, operating in the subsonic flight regime.

References

[1] Saville, O.B.O. "Adaptive Evolution in the Avian Wing," *Evolution*, Vol 11, No. 2, 1957, pp. 212-224.

[2] Burgers, P. and Chiappe, L.M., "The Wing of Archaeopteryx as a Primary Thrust Generator," *Nature*, Vol 399, no. 6731, pp. 60.

[3] Lanchester, F.W., "Aerodynamics-Constituting the First Volume of a Complete Work on Aerial Flight," *A. Constable and Co., Ltd*, 1907.

[4] Prandtl, L.,"On Wings with Minimum Induced Drag," *Ũber Tragflugel kleinsten induzierten Widerstandes*, Vol. 24, pp. 305-306, 1932

[5] Klein, A., and Viswanathan, S.P., "Approximate Solution for Minimum Induced Drag of Wings with Given Structural Weight," *Journal of Aircraft*, Vol. 12, No. 2, pp. 124-126, 1975.

[6] Van Dam, C.P., "Induced-Drag Characteristics of Crescent-Moon-Shaped Wings," *Journal of Aircraft*, Vol. 24, No. 2, pp. 115-119, 1987.

[7] Jones, R.T., "The Spanwise Distribution of Lift for Minimum Induced Drag of Wings Having a Given Lift and a Given Bending Moment," *NACA TN-2249*, 1950.

[8] Munk, M.M., "The Minimum Induced Drag of Aerofoils," *NACA Report 121*, 1923

[9] Kroo, I., "Nonplanar Wing Concepts for Increased Aircraft Efficiency," *VKI lecture series on innovative configurations and advanced concepts for future civil aircraft*, pp. 6-10, 2005.

[10] Whitcomb, R.T., "A Design Approach and Selected Wing Tunnel Results at High Subsonic Speeds for Wing-Tip Mounted Winglets," 1976.

[11] Standinford, D.W.F., and E.O. Tuck., "Optimal Rectangular End Plates," *Journal of Aircraft*, Vol. 33, No. 3, 1996.

[12] Vogt, R., U.S. Patent for "Twisted Wing Top Fin", No. 2, pp. 567-981, filed 1951.

[13] Heller, G. Fiarchild Dornier, Wessling, Germany, US Patent for " Wing Tip Extension for a Wing,"

No. 6,72,615, Filed 2002.

[14] Jarvis, J., and Selberg, B., " Investigation of Aerodynamic Improvements Using Wing Tip Sails, " *AIAA Paper 1999-530*, 1999

[15] Nangia, R. K., M. E. Palmer, and C. P. Tilmann. "Unconventional High Aspect Ratio Joined-Wing Aircraft with Aft and Forward Swept Wing Tips, *AIAA Paper 2003-0506*

[16] Maughmer, M. D., "Design of winglets for high-performance sailplanes", *Journal of Aircraft*, Vol 40, No. 6, pp. 1099-1106, 2003.

[17] Rokhsaz, K., "A Brief Survey of Wing Tip Devices for Drag Reduction," *SAE Technical Paper*, No. 932574, 1993.

[18] Norton, F.H., "An Investigation on the Effect of Raked Wing tips," *Technical Notes : National Advisory Committee for Aeronautics*, No. 69, 1921.

[19] Brennan, J. E., "Aerodynamic Effects of Wingtip-Mounted Propellers and Turbines," *AIAA Paper 1986-1802*, 1986

[20] Vogel, J.M., "An Application of the Ogee Tip," *Proceedings of NASA-Industry-University-General-Aviation Drag Reduction Workshop*, University of Kansas, Lawrence, KS., 1975.

[21] Vijgen, P.M.H.W, Van Dam, C.P., and B. Holmes., "Sheared Wing-Tip Aerodynamics: Wind Tunnel and Computational Investigation," *Journal of Aircraft*, Vol. 26, No. 3, 1989.

[22] Prandtl, L., "Induced Drag of Multiplanes," *NACA TB 182*, From Technische Berichte, Vol. 3, No. 7., pp. 309-315, 1924

[23] Cavallaro, R.,and Demasi, L., "Challenges, ideas, and innovations of joined-wing configurations: a concept from the past, an opportunity for the future," *Progress in Aerospace Sciences*, Vol. 87, pp. 1-93, 2016

[24] Corsiglia, V.R., Rossow, V.J., and Ciffone, D.L., "Experimental Study of the Effect of Span Loading on Aircraft Wakes," *Journal of Aircraft*, Vol. 13, No. 12, 1976 , pp. 968-973

[25] Croom, D.R., and Dunbam, Jr, .R.E., "Low Speed Wind Tunnel Investigation of Span Load Alteration, Forward-Located Spoilers, and Splines as Trailing-Vortex-Hazard Alleviation Devices on a Transport Model," *NASA TN D-8133*, 1975

[26] Croom, D.R., "Low-Speed ind Tunnel Investigation of Flight Spoilers as Trailing Vortex Hazard-Alleviation Devices on a Transport Aircraft Model," *NASA TN D-8162*, 1976

[27] Barber, M.R., Hastings, E.C., Champine, R.A., and Tymczyszyn, J.J., "Vortex Attenuation Flight Experiments, Wake Vortex Minimization," *NASA SP-409*, 1977

[28] Rossow, V.J., " On the Inviscid Rolled-up Structure of Lift-Generated Devices," *Journal of Aircraft*,

Vol. 10, 1973, pp. 86-92

[29] Rossow, V.J., "Theoretical Study of Lift-Generated Vortex Wakes Designed to Avoid Rollup," *AIAA Journal*, Vol. 13, No. 4, 1975, pp. 476-484

[30] Rossow, V.J., "Inviscid Modeling of Aircraft Trailing Vortices, Wake Vortex Minimization," *NASA SP-409*, 1977

[31] Chigier, N.A. and Corsiglia, V.R., "Tip Vortices-Velocity Distribution," *NASA TM X-62087*, 1971

[32] Chigier, N.A. and Corsiglia, V.R., "Wind Tunnel Studies of Wing Wake Turbulence," *Journal of Aircraft*, Vol. 9, No. 12, 1972, pp. 820-825

[33] Kirkman, K.L., Brown, C.E., and Goodman, A., "Evaluation of Effectiveness of Various Devices for Attenuation of Trailing Vortices Based on Model Tests in a Large Towing Basin,", *NASA R-22-2*, 1973

[34] Patterson, J.C., "Vortex Attenuation Obtained in the Langely Vortex Research Facility," *Journal of Aircraft*, Vol. 12, No. 9, 1975, pp. 745-749

[35] Smith, H.J., " A Flight Test Investigation of The Rolling Moments Induced on a T-37B Airplane in The Wake of a B-747 Airplane," *NASA TM X-56031*, 1975

[36] Ranjan, P. and Ansell, P.J., "Computational Analysis of Vortex Wakes Without Near-Field Rollup Characteristics," *Journal of Aircraft*, pp. 1-14, 2018.

[37] Wroblewski, G.E. and Ansell, P.J., "Prediction and Experimental Evaluation of Planar Wing Spanloads for Minimum Drag,"*Journal of Aircraft*, Vol. 54, No. 5, pp. 1664-1674, 2017.

[38] Hicks, R.M. and Henne, P.A., "Wing Design by Numerical Optimization," *Journal of Aircraft*, Vol. 15, No. 7, pp. 407-412, 1978.

[39] Vicini, A. and Quagliarella, D., "Airfoil and Wing Design Through Hybrid Optimization Strategies, " *AIAA Journal*, Vol. 37, No. 5, pp. 634-641, 1999.

[40] Keane, A.J., "Wing optimization Using Design of Experiment, Response Surface, and Data Fusion Methods, " *Journal of Aircraft*, Vol. 40, No. 4, pp. 741-750, 2003.

[41] Sobieszczanski-Sobieski, J. and Haftka, R. T., " Multidisciplinary Aerospace Design Optimization: Survey of Recent Developments," *Structural Optimization*, Vol. 14, No. 1, pp. 1- 23, 1997.

[42] James, K. A., Kennedy, G. J., and Martins, J. R., "Concurrent Aerostructural Topology Optimization of a Wing Box, " *Computers and Structures*, Vol. 134, pp. 1-17, 2014.

[43] Martins, J. R. R. A., Alonso, J. J., and Reuther, J. J., " High-Fidelity Aerostructural Design Optimization of a Supersonic Business Jet," *Journal of Aircraft*, Vol. 41, No. 3, pp. 523-530, 2004.

[44] Maute, K., and Reich, G. W., "Integrated Multidisciplinary Topology Optimization Approach to Adaptive Wing Design, " *Journal of Aircraft*, Vol. 43, No. 1, pp. 253-263, 2006.

[45] Jansen, P. W., Perez, R. E., and RA Martins, J. R., "Aerostructural optimization of nonplanar lifting surfaces," *Journal of Aircraft*, Vol. 47, No. 5, pp. 1490-1503, 2010

[46] Reynolds, K. and Nguyen, N., "Multi-Objective Wing Shape Optimization of an Elastically-Shaped Aircraft Concept," *AIAA paper 2013-0142*, 2013.

[47] Cone Jr, C. D., "The Theory of Induced Lift and Minimum Induced Drag of Nonplanar Lifting Systems", 1962.

[48] Lazos, B.S., "Biologically Inspired Fixed-Wing Configuration Studies," *Journal of Aircraft*, Vol. 42, No. 5, 2005.

[49] Lazos, B.S. and Visser, K.D., "Aerodynamic Comparison of Hyper-Elliptic Cambered Span (HECS) Wings with Conventional Configurations," *AIAA Paper 2006-3469*, 2006.

[50] Lowson, M., "Minimum Induced Drag for Wings with Spanwise Camber," *Journal of Aircraft*, Vol 27, No. 7, pp. 627-631, 1990.

[51] Lundry, J.L., and Lissaman, P.B.S., "A Numerical Solution for the Minimum Induced Drag of Nonplanar Wings," *Journal of Aircraft*, Vol. 5, No. 1., 1968.

[52] Lierch, C.M., Streit, T., and Visser, K.D., "Numerical implications of spanwise camber on minimum induced drag configurations," *AIAA Paper 2009-898*, 2009

[53] Pomeroy, Brent W., and Kenneth D. Visser. "A Computational Study of Induced Drag Behavior for Spanwise Cambered Wings." *AIAA Paper 2010-4227*, 2010.

[54] Lee, M.W. and Visser, K.D., "Towards an Effective Nonplanar Wing Design Strategy," *2016-4328*, 2016

[55] Blackwell, J. A., Jr., "Numerical Method to Calculate the Induced Drag or Optimum Loading for Arbitrary Non-Planar Aircraft," *NASA SP-405*, 1976

[56] Igleasis, S. and Mason, W.H., "Optimum Spanloads Incorporating Wing Structural Weight," *AIAA Paper 2001-5234*, 2001.

[57] Ning, S.A., and Kroo, I., "Multidisciplinary Considerations in the Design of Wings and Wing-Tip Devices," *Journal of Aircraft*, Vol. 47, No. 2, 2010, pp. 534-543

[58] Verstraeten, J.G., and Slingerland, R., "Drag Characteristics for Optimally Span-Loaded Planar Wingletted and C Wings," *Journal of Aircraft*, Vol. 46, No. 3, 2009, pp. 81-99

[59] Kroo, I., "A General Approach to Multiple Lifting Surface Design and Analysis," *AIAA Paper 1984-2507*, 1984.

[60] Demasi, L., Monegato, G., and Cavallaro, R. ,"Minimum induced drag theorems for multi-wing systems," *In 57th AIAA/ASCE/AHS/ASC Structures, Structural Dynamics, and Materials Conference,* p. 0236, 2016

[61] Demasi, L., Monegato, G., Rizzo, E., Cavallaro, R., and Dipace, A., "Minimum induced drag theorems for joined wings, closed systems, and generic biwings: Applications. Journal of Optimization Theory and Applications, Vol. 169, No. 1, pp. 236-261, 2016

[62] Potra, F.A., and Wright, S.J., "Interior-Point Methods," *Journal of Computational and Applied Mathematics*, Vol. 126, No.1, pp. 281-302, 2000

[63] Versteeg, H.K., and Malalasekera, M., "The Finite Volume Method," *An Introduction to Computational Fluid Dynamics : Longman Scientific and Technical*, 1995

[64] Weller, H.G, Tabor, G, Jasak, H and Fureby, C, "A tensorial approach to computational continuum mechanics using object-oriented technique," *Computers in Physics*, Vol. 12, No. 6, 1998

[65] Ferziger, J.H. and Peric, M, "Further Discussion of Numerical Errors in CFD ," *International Journal for Numerical Methods in Fluids*, Vol. 23, No. 12, pp. 1263-1274, 1996

[66] Forde, B. W., Foschi, R. O., and Stiemer, S. F., "Object-Oriented Finite Element Analysis," *Computers and Structures*, Vol. 34, No.3, ,pp. 355-374, 1990

[67] Gomez, S., Graves, B.J. and Poroseva, S.V., "On the Accuracy of RANS simulations of 2D boundary Layers with OpenFOAM," *AIAA paper 2014-2087*, 2014

[68] Habbit, R.D., Porteus, A.,B., Exhavarria, C.M.L, Poroseva, S.V., and Murman, S.M., "Computational Analysis of Two-Dimensional Flows with OpenFOAM," *2015-0519*, 2015

[69] Doolan, C., "Flow and Noise Simulation of the NASA Tandem Cylinder Experiment using OpenFOAM," *AIAA paper 2009-3157*, 2009.

[70] Balogh, M., Parente, A. and Benocci, C., "RANS Simulation of ABL Flow Over Complex Terrains Applying an Enhanced k-Îţ Model and Wall Function Formulation: Implementation and Comparison for Fluent and OpenFOAM," *Journal of wind engineering and industrial aerodynamics*, Vol. 104, pp. 360-368, 2012

[71] Muntean, S., Nilsson, H. and Susan-Resiga, R.F., "3D Numerical Analysis of the Unsteady Turbulent Swirling Flow in a Conical Diffuser using Fluent and OpenFOAM," *In Proceedings of the 3rd IAHR International Meeting of the Workgroup on Cavitation and Dynamic Problems in Hydraulic Machinery and Systems*, pp. 14-16, 2009

[72] Mack, A. and Spruijt, M.P.N., "Validation of OpenFoam for Heavy Gas Dispersion Applications," *Journal of hazardous materials*, Vol. 262, pp. 504-516, 2013

[73] Kanoria, A.A. and Chandar, D.D., "Integrating the Stanford University Unstructured Code (SU2) With Overset Grids," *AIAA paper 2015-3428*, 2015

[74] Liu, Q., Gomez, F., Perez, J.M. and Theofilis, V., "Instability and Sensitivity Analysis of Flows Using

OpenFOAM," *Chinese Journal of Aeronautics*, Vol. 29, No. 2, pp. 316-325, 2016

[75] Furbo, E., "Evaluation of RANS Turbulence Models for Flow Problems with Significant Impact of Boundary Layers," *Master's thesis: Teknisk naturvetenskaplig fakultet UTH enheten*, 2010.

[76] Walters, D.K. and Cokljat, D., "A Three- Equation Eddy-Viscosity Model for Reynolds-Averaged Navier-Stokes Simulations of Transitional Flow," *Journal of Fluids Engineering*, Vol. 130, 2008

[77] Mayle, R.E. and Schulz, A., "The path to Predicting Bypass Transition," *ASME Journal of Turbomachinery*, Vol. 128, pp. 413-422, 2006

[78] Walters, D.K., and Leylek, J.H., "A New Model for Boundary Layer Transition Using a Single-Point RANS Approach," *ASME Journal of Turbo machinery*, Vol. 126, pp. 67- 79, 2002

[79] Furst, J., "Numerical Simulation of Transitional Flows with Laminar Kinetic Energy," *Engineering Mechanics*, Vol. 20, No. 5, pp. 379-388, 2013

[80] Coder, James G., and Mark D. Maughmer, "A CFD-compatible transition model using an amplification factor transport equation," AIAA Paper 2013-0253, 2013